Optical Engineering

OpticalEngineering.SPIEDigitalLibrary.org

Design considerations for an optical link supporting intersatellite quantum key distribution

Denis Naughton
Robert Bedington
Simon Barraclough
Tanvirul Islam
Doug Griffin
Brenton Smith
Joe Kurtz
Andrey S. Alenin
Israel J. Vaughn
Arvind Ramana
Igor Dimitrijevic
Zong Sheng Tang
Christian Kurtsiefer
Alexander Ling
Russell Boyce

Denis Naughton, Robert Bedington, Simon Barraclough, Tanvirul Islam, Doug Griffin, Brenton Smith, Joe Kurtz, Andrey S. Alenin, Israel J. Vaughn, Arvind Ramana, Igor Dimitrijevic, Zong Sheng Tang, Christian Kurtsiefer, Alexander Ling, Russell Boyce, “Design considerations for an optical link supporting intersatellite quantum key distribution,” *Opt. Eng.* **58**(1), 016106 (2019), doi: 10.1117/1.OE.58.1.016106.

Optical Engineering 58(1), 016106 (January 2019)

Design considerations for an optical link supporting intersatellite quantum key distribution

Denis Naughton,[a,*] Robert Bedington,[b] Simon Barraclough,[a] Tanvirul Islam,[b] Doug Griffin,[a] Brenton Smith,[a] Joe Kurtz,[a] Andrey S. Alenin,[a] Israel J. Vaughn,[a] Arvind Ramana,[a] Igor Dimitrijevic,[a] Zong Sheng Tang,[b] Christian Kurtsiefer,[b,c] Alexander Ling,[b,c] and Russell Boyce[a]
[a]University of New South Wales Canberra, School of Engineering and Information Technology, Canberra, Australia
[b]National University of Singapore, Centre for Quantum Technologies, Singapore
[c]National University of Singapore, Department of Physics, Singapore

Abstract. Quantum key distribution (QKD) is a method for establishing secure cryptographic keys between two parties who share an optical, "quantum" channel and an authenticated classical channel. To share such keys across the globe, space-based links are required and in the near term these will take the form of trusted node, key management satellites. We consider such channels between two nanosatellite spacecraft for polarization entanglement-based QKD, and the optical channel is described in detail. Quantum channels between satellites are useful for balancing keys within constellations of trusted node QKD satellites and, in the future, may have applications in long-distance qubit exchange between quantum computers and in fundamental physics experiments. The nanosatellite mission proposed uses an optical link with 80-mm diameter optical terminals. If such a link could be maintained with 10-μrad pointing accuracy, then this would allow QKD to be performed for satellite separations up to around 400 km. A potential pointing and tracking system is also described although currently this design would likely limit the satellite separation to 100 to 150 km. [DOI: 10.1117/1.OE.58.1.016106]

Keywords: intersatellite link; quantum key distribution; entanglement; CubeSat.

Paper 181192SS received Aug. 16, 2018; accepted for publication Oct. 10, 2018; published online Jan. 9, 2019.

1 Introduction

There is a growing interest in applications where quantum information is transmitted between distant locations. These applications often require the exchange of quantum states, sometimes including the distribution of quantum entanglement.[1] Furthermore, long-range entanglement distribution has the potential to enable new fundamental physics experiments.[2,3] As quantum states are extremely sensitive to system noise and transmission loss, long-distance links via satellite nodes are especially attractive compared with fiber optic and ground-based alternatives.[4–7]

Recently, there has been progress in demonstrating satellite to ground quantum communication,[8–11] which is the only scenario that has thus far been demonstrated. However, achieving quantum communication between many satellites—a necessary element of large-scale quantum networks—is yet to be demonstrated. Future networks will require both satellite-to-satellite and satellite-to-ground links. There are several configurations for performing QKD between satellites and ground stations depending on the types of links that are used.[12] It is conceivable that CubeSats can serve as both the transmit and receive nodes in a satellite to ground scenario. However, improvements in CubeSat orientation and stability maintenance will be needed.[13,14]

Although these networks may ultimately require links of thousands of kilometers, a first step is to demonstrate shorter range quantum communication between two nanosatellites in low Earth orbit (LEO). In this work, we present a pathfinder mission architecture based on two 6U ($10\ \text{cm} \times 20\ \text{cm} \times 30\ \text{cm}$) CubeSats. The choice of CubeSats as the satellite platform reduces the overall cost of the mission. However, due to their size and mass constraints, producing a suitable optical link between them becomes technically challenging and limited to a few hundred kilometers.

As quantum key distribution (QKD) is the most mature form of quantum communication, we use it as a baseline to define the mission and system requirements. We are targeting polarization entanglement-based QKD, but the system is equally applicable to most other forms of QKD.

1.1 *Quantum Key Distribution*

QKD uses physical properties of light to distribute randomized or entangled quantum states between two distant parties, enabling them to establish shared secret encryption keys.[15,16] As any attempt to measure an unknown quantum state necessarily perturbs it, any such intrusion by an eavesdropper can be detected. Moreover, an unknown quantum state cannot be cloned so an eavesdropper cannot save a copy of the state to gain information about the secret key, preventing man-in-the-middle attacks. These guarantees are derived from the postulates of quantum mechanics; therefore, unlike classical key distribution, QKD can be proven to be secure without any computational assumption.[17]

There are several approaches to achieve QKD over optical links and entanglement is not required for all of them, but nonentanglement-based QKD approaches require a trusted random number generator to perform the protocols. In

---

*Address all correspondence to: Denis Naughton, E-mail: d.naughton@unsw.edu.au

contrast, with entanglement-based QKD, the randomness is intrinsic to the quantum process. Furthermore, an entanglement-based QKD system can natively supply the means for clock synchronization between the communicating parties.[18] This reduces the number of trusted components that must be incorporated into the overall system.

In entanglement-based QKD, pairs of entangled photons are generated and sent to two separate parties, such that each party is sent one photon from each pair. The two parties independently make measurements on a preselected property of the photons (e.g., their polarization state). Once many such pairs have been distributed and measured, the two parties can perform statistical tests and discuss publicly if the photons they received were entangled. Provided the entanglement measured exceeds a calculated threshold and their hardware is free from vulnerabilities, they can be certain of the security of the protocol. They can then use their private knowledge of the quantum states—information that has not been publicly shared—as a common source of entropy from which to derive symmetric keying material for encryption schemes.

In this study, we use the BBM92 protocol,[19] which is procedurally equivalent to the older BB84 protocol[20] but uses entangled photon pairs instead of weak laser pulses. Satellite-based QKD is currently in its infancy; the first fully operational QKD satellite, Micius, developed by the Chinese Academy of Sciences, demonstrated space-to-ground QKD and entanglement distribution in 2017,[8,21,22] but many more missions are in development.[4]

1.2 *Intersatellite Optical Links*

A single QKD satellite in a polar orbit can, in principle, serve the entire planet, but to serve large numbers of users in reasonable timescales, constellations of satellites will be required and for any near-term implementation, these satellites would operate as trusted key management nodes.[4] Such satellite nodes would establish a cache of keys with the ground stations they pass over and, via an RF relay, XOR keys from their cache on demand to allow any two ground stations to establish symmetric keys. While such satellites could all operate independently of each other, if the satellites feature intersatellite QKD crosslinks they are able to balance the keys in their caches to allow for more efficient operations.

Intersatellite optical communication systems and technologies have undergone performance developments and enhancements for several decades.[23] Satellite QKD is essentially a specialized version of free space optics (FSO) communications,[24] and the performance capacity of these future systems will be limited primarily by diffraction spreading of the transmitted beam and by the line-of sight (LOS) errors caused by inaccuracies and disturbances generated within the optical transceivers. To mitigate these performance degradation factors, conventional, space-based FSO systems are designed with gimbal-based telescopes to provide course and fine tracking functions.[25–27] Establishing even a traditional optical link between CubeSats is more challenging as the size, weight, and power (SWaP) constraints limit the size of the optical transceivers. We are not aware of any publications on inter-CubeSat QKD, although recent efforts to enable classical optical communications from CubeSats to ground[28,29] and between CubeSats have been reported.[30]

There are several technological challenges that impact the overall feasibility of any intersatellite quantum communications. These include noise in the receiver path due to stray light, which potentially limits daytime QKD transmission,[31] diffraction that degrades the optical link margin and therefore places limits on the achievable secure key generation rates and the provision of a pointing, acquisition, and tracking subsystem (PATS) to maintain alignment between the transmitter and receiver as the spacecraft are in a constant motion.[32]

2 Mission Overview

The mission objectives of this study are to demonstrate entanglement distribution and QKD over extended ranges between two CubeSats in LEO, to raise the technology readiness level (TRL) of enabling technologies for nanosatellite-based FSO communications systems, and to validate system design parameters and performance models that will support the design of future global quantum communication systems.

The mission design features two 6U CubeSats, each carrying a source of polarization-entangled photon pairs and an optical transceiver while flying in the formation at varying separations. Conceptually, entanglement distribution and QKD only require that the quantum states travel in one direction, i.e., they only require that one spacecraft should be the entangled photon transmitter and the other be the receiver. However, in a future operational network with three or more spacecraft, it is envisioned that spacecraft would be capable of both sending and receiving polarization-entangled photons. For our mission, a single direction is the key requirement, but a bidirectional capability is considered desirable as it would add redundancy to operations, allow the design of the two spacecraft to be nearly identical, and more closely demonstrate the capabilities that might be required for a future constellation-based node.

The following sections introduce the concept of the mission operations and the spacecraft, the optical communications subsystems, the quantum module (QM), and its detector cooling system.

2.1 *Mission Operations*

During the on-orbit commissioning phase, the spacecraft systems can be tested prior to separation, thus enabling verification of the quantum link at the start of spacecraft commissioning. This led to a design configuration, where the two 6U spacecraft are launched as a single composite 12U spacecraft. The spacecraft is injected into an initial sun-synchronous circular orbit at an altitude between 500 and 550 km (LTDN 10:30) and upon separation they are steered into their operational positions as shown in Fig. 1.

During the mission, differential drag maneuvers are used to control the relative velocity of the spacecraft. One spacecraft is commanded to a maximum drag attitude and the other spacecraft to a minimum drag attitude. The total orbital energy of one spacecraft will then decrease more rapidly than the other and cause it to drop to a lower altitude while attaining a higher velocity and shorter orbital period.[33] Once a constant relative separation velocity of $\sim 10\ \mathrm{cm/s}$ is achieved, QKD operations can begin.

As the separation range increases, the photon detection rate decreases as the free-space losses increase with the separation distance. As the SNR drops, there will come a

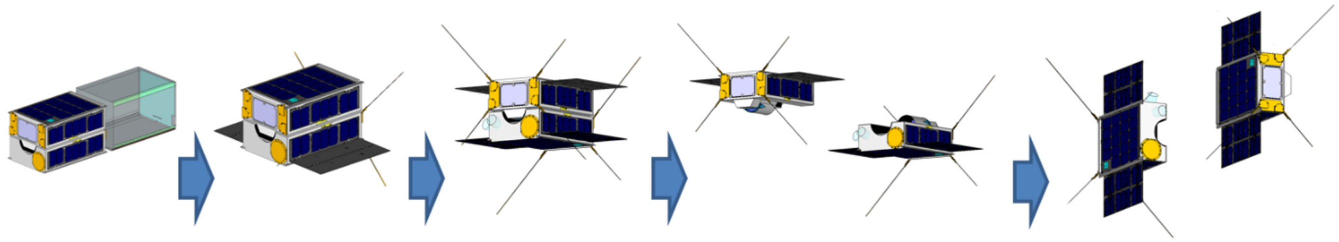

Fig. 1 Spacecraft deployment and separation sequence. They are deployed as a single 12U CubeSat, which, after functional checks, separates into two 6U spacecraft. These are then maneuvered to fly in formation.

point where the percentage of errors in the quantum measurements—the quantum-bit-error-rate (QBER)—will exceed a threshold above which BBM92 QKD[19,34] cannot be realized. Beyond the corresponding separation distance, it should still be possible to perform entanglement distribution demonstrations.

The mission concept is that QKD will be conducted when the spacecraft are in eclipse to minimize noise due to scattered sunlight. With further developments, daylight QKD links[35] may be possible, but significant technology challenges remain to develop future operational QKD service networks.[31,36]

2.2 *Spacecraft Concept*

Both satellites will have a QM, which can both send and receive entangled signal photons. The two satellites will also use a beacon laser and a beacon tracking detector (BTD) to monitor the other satellite's beacon and control the relative pointing between them. The centroid of the received beacon is determined relative to the boresight of the receiver and a beam pointing correction signal is provided to a two-axis fast steering mirror (FSM). The FSM compensates for high-frequency beam misalignment between the two spacecraft and optimizes the optical link for the transmission of entangled photons. The optical link and spacecraft elements are envisioned as a combination of commercial and custom components.

Figure 2 shows a layout of the key spacecraft and payload subsystems that are supported on an optical bench. The optical bench provides thermal and mechanical isolations and is attached to the spacecraft structure via a three-point mount scheme. The spacecraft platform subsystems are organized within the remaining volume and are shown in Table 1.

The orientation of the two 6U satellites in the launch volume is shown in Fig. 3. The launch packing arrangement positions the telescopes with their boresights co-aligned allowing the optical links to be tested prior to the spacecraft separating and facilitates the alignment of the spacecraft and checks of on-orbit functionality.

The reaction wheels (RW) have been placed, so that their spin axes are as near as possible to the center of gravity to minimize jitter on the pointing stability of the telescope.

2.3 *Quantum Module*

Each CubeSat contains a QM composed of a miniaturized polarization entangled photon pair source[12,37] and single-photon detectors. The transmitting QM locally measures and timestamps one of the photons in each pair and sends the other photon in each pair to the receiver spacecraft, where it is detected and timestamped by a nearly identical receiving QM.[18] These timestamp and measurement

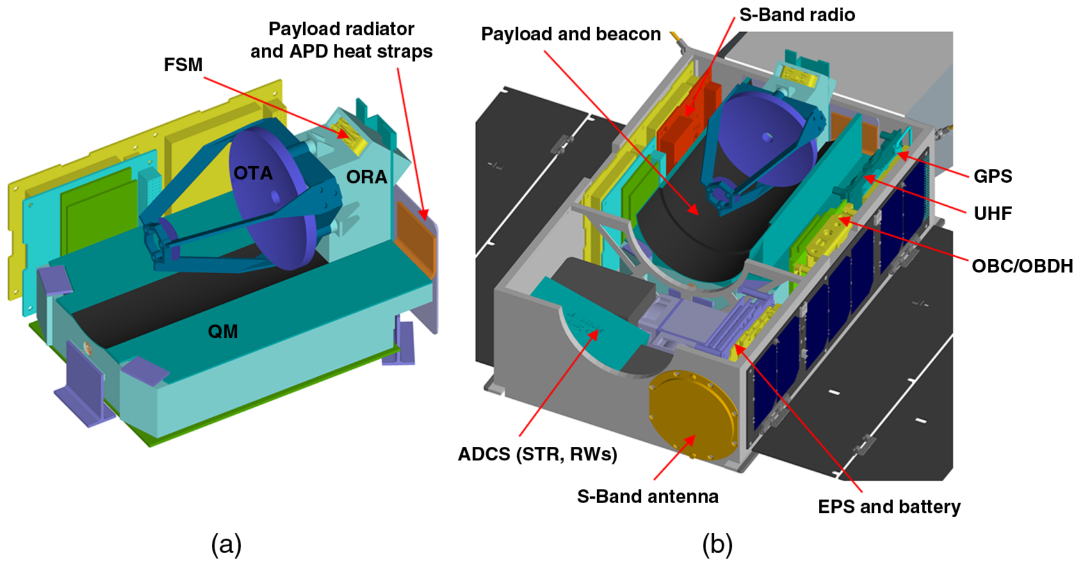

Fig. 2 (a) Layout of the main optical payload and (b) the block configuration of the 6U spacecraft including main platform subsystems.

Table 1 Acronym glossary and functional description of spacecraft and payload subsystems.

Spacecraft subsystems	Function
Electrical power system (EPS)	The EPS provides conditioned power to all spacecraft and payload subsystems and interfaces to all power sources including the solar arrays and batteries.
Batteries	Rechargeable batteries that store energy for the operation of the spacecraft.
On-board computer (OBC)	Monitors and controls the real-time operations of the spacecraft and its subsystems.
ADCS	Includes a combination of units, such as star trackers, RW, torque rods and electronics to provide spacecraft stabilization and pointing capability, as well as rate, attitude, position and velocity control and knowledge.
UHF radio and antenna	Ultrahigh-frequency two-way radio and antenna subsystem providing telemetry and command and control communications.
S-band radio and antenna	*S*-band radio and antenna providing higher speed data downlink capability.
GPS receiver	Global Positioning System unit to receive and decode GPS satellite data and communicate it to the OBC. Used for orbit verification and timing.
Solar arrays	Stowed deployable panels containing solar cells for power generation.
Payload subsystems	**Function**
QM	A polarization-entangled photon pair source and single-photon detectors that can operate as a qubit transmitter or receiver.
TCS	Passive cooling system for cooling the single-photon detectors in the QM.
OTA	Quantum transceiver telescope for the signal photons. It also acts as the receiver for an optical tracking beacon.
BTD	A CMOS detector which allows the spacecraft to locate and coalign their respective telescope boresights at large separations.
Optical relay assembly (ORA)	Routes signal photons between QM and OTA and incoming beacon light from OTA to the BTD.
FSM	Located within the ORA, a two-axis FSM enables fine beam pointing adjustments in the shared optical path of the signal photons and the incoming beacon using a feedback control signal generated from the BTD.
BTA	A separate telescope used for transmitting the tracking beacon.
Optical beacon assembly	Assembly that couples the beacon light to the beacon telescope via an optical fiber.

outcomes are used to synchronize the detections and subsequently to create a symmetric encryption key.

The QM contains a 405-nm laser diode as the pump source that initiates spontaneous-parametric-down-conversion[38] in beta-barium-borate crystals generating pairs of photons with wavelengths of 760 and 867 nm, respectively. The photons in each pair are entangled such that their individual polarization states are undefined until a measurement is made, at which point they will have correlated polarizations. In the transmitter QM, 760-nm "signal" photons are transmitted out of the spacecraft and the 867-nm "idler" photons are detected within the QM by silicon avalanche photo diodes (APDs) operating in a Geiger mode (GM-APDs). The basic layout of the QM is shown in Fig. 4.

The QM output flux in this study was estimated at 5×10^6 photons per second, or equivalently ∼125 pW at 760 nm.[12] This rate must be matched by the detector unit, which is currently the limiting factor to speed increases. The receiver QM detects 760-nm photons, and, in future design iterations, it is intended for it to be able to transmit 867-nm photons (and for the other QM to be able to receive 867-nm photons) for reversing the transmitter and receiver roles.

2.4 *Detector Cooling System*

GM-APDs are often cooled with thermoelectric coolers; however, for power- and heat-management reasons, CubeSat thermal control subsystems (TCS) are typically passive and control the temperature of critical items by providing internal thermal resistances and inertias. Accordingly, the baseline design features a dedicated deployable radiator connected to the APDs using copper straps and low surface area mounts between the QM and the optical bench [reference Fig. 2(a)]. A deployable baffle (shown in Fig. 5) and a low emissivity reflective finish on the radiator minimize heating by infrared radiation.

The on-orbit thermal performance of the spacecraft has been modeled analytically using finite difference models produced in ESATAN-TMS.[39] The spacecraft model contains 244 shells representing the structure, optical subsystems, solar arrays, RF antennas, and external panels. The surface material thermo-optical properties, heat sources, thermal couplings, and the spacecraft geometric model are also modeled. The output is a set of predicted temperature values for various thermal load conditions experienced by the spacecraft in its orbit. The worst-case temperatures predicted during the mission allow an assessment of the system performance and indicate that the TCS can lower operational temperatures of the APDs to $\sim -10°\text{C}$. In many cases, it is desirable to lower APD temperatures to $-20°\text{C}$ or even $-30°\text{C}$ to further suppress dark counts, especially as dark counts increase with radiation damage.[40] In this design study, however, it will be seen that detector noise is not the limiting factor in the achievable range for the two satellites.

3 Optical Link Analysis

The link margin of a classical optical communications channel characterizes the signal to noise properties of the channel and predicts the level of bit errors and channel dropouts that may occur. For a QKD channel, the QBER is used as the principle link performance metric and for BBM92 QKD,

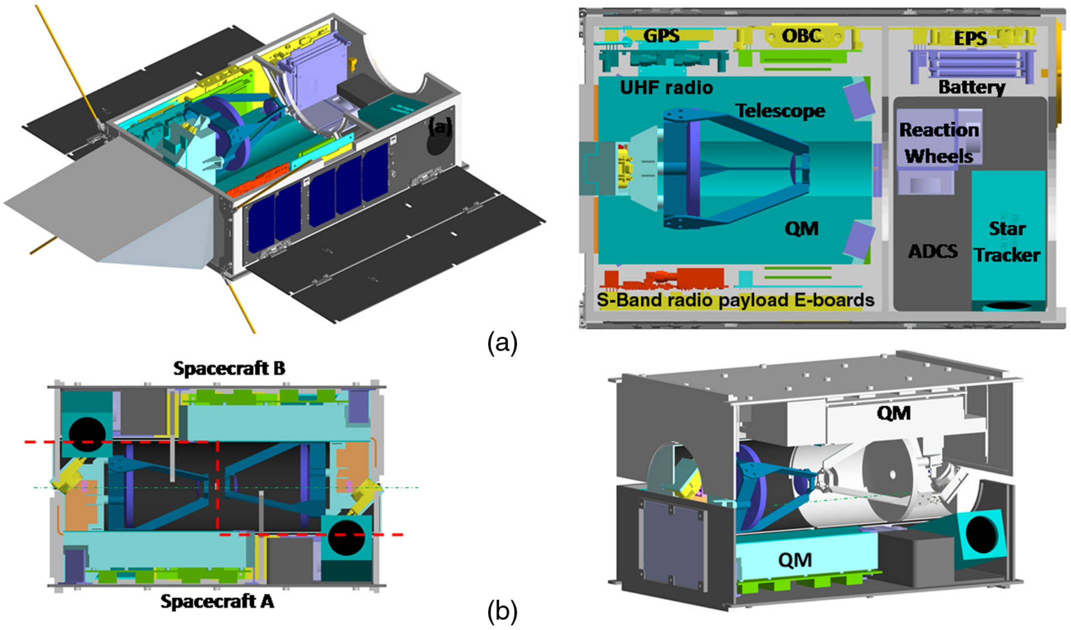

Fig. 3 (a) Layout of one spacecraft and location of its subsystems. (b) View of both spacecraft in their pre-launch configuration; the thick dashed line indicating the division between the two. In this configuration the telescope boresights are aligned, as indicated by the thin dashed line, allowing for end-to-end functional testing.

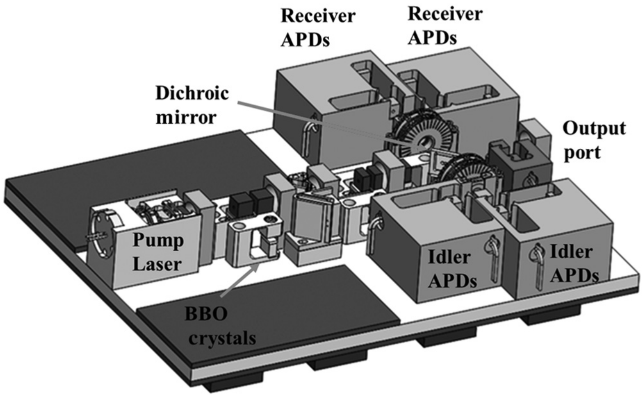

Fig. 4 QM components, with cover removed. Four APD polarization analyzers and liquid crystal rotator for sampling the output beam are indicated. Sections indicating the electronics and high-voltage power supplies for the detectors are mounted on the underside of the module.

a QBER of ∼11% is an upper limit for secure key distribution.[34] Transmission losses and noise both contribute to increasing QBER. As mentioned previously, detector noise can be reduced if the temperature of the APDs is lowered, thereby reducing the dark counts that allow for higher transmission losses to be tolerated.[32,41]

Figure 6 shows the QBER for our system as a function of link attenuation in dB for varying APD detector operating temperatures. For example, at an APD operating temperature of −10°C the link loss corresponding to the QBER threshold of 11% is ∼39 dB. The thermal model shows that the APD could be cooled to this temperature and established a working limit for the optical link loss in the system. It should be noted, however, that at the 11% QBER limit the secure key rate is zero, so lower limits would need to be imposed for practical applications. For scientific applications, however, the range might be slightly longer as quantum entanglement distribution experiments based on the outcome of entanglement witnesses could, in principle, continue up to a QBER threshold of ∼14.6%.[42]

Optical communication links require very precise pointing compared with RF communication links. Aligning the two telescopes in this mission to point and track each other is achieved coarsely by orienting the entire spacecraft using the attitude determination control system (ADCS) and finely through the use of an FSM that tracks the beacon from the partner spacecraft.

The link equation from antenna theory is a suitable model for predicting the performance of an FSO communications channel and provides a framework for component selection.[43] The equation describes the amount of power at a receiver as a function of the transmitter and receiver gains, and the signal losses due to optical system throughput, free space propagation, atmospheric scattering, and absorption and uncompensated pointing error.

It can be written as

$$P_R = P_T * G_T * n_T * L_{ptg} * L_{FS} * G_R * n_R * L_{atm},$$

where P_R is the power measured at the receiver, P_T is the power transmitted by the source, G_T is the gain of the transmitter, η_T is the transmitter optical throughput loss, L_{ptg} is the loss due to pointing errors between the transmitter and receiver, L_{FS} is the loss due to free-space transmission (diffraction loss), $=[\lambda/(4\pi R)]^2$, R is the separation between Rx and Tx (range), λ is the wavelength, G_R is the gain of the receiver, η_R is the receiver optical throughput loss, and L_{atm} is the loss due to atmospheric scattering and absorption.

The predicted optical losses do not include stray light, polarization losses, and atmospheric scattering losses.

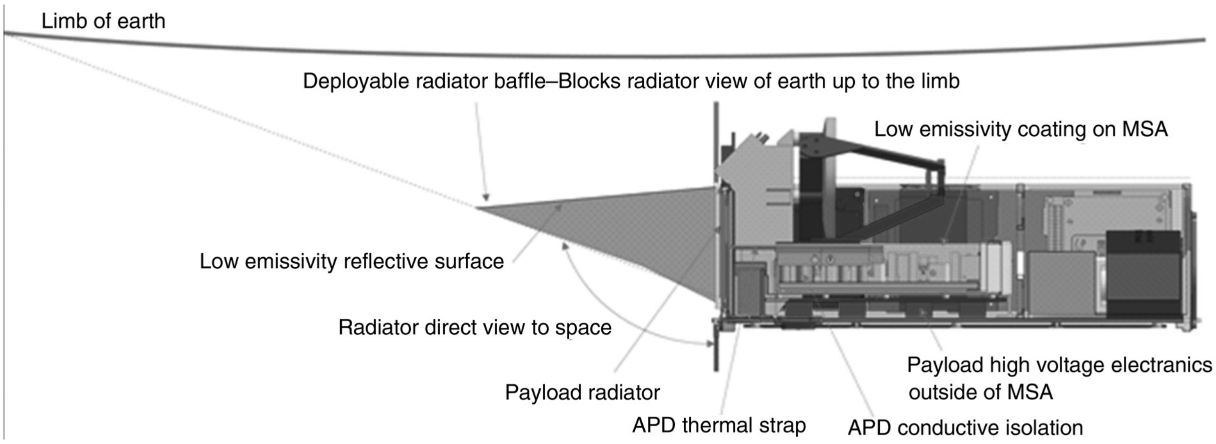

Fig. 5 The spacecraft requires only passive thermal control features. The APDs are connected by a thermal strap to a radiator, which is shielded from external radiative heat sources by a deployable baffle.

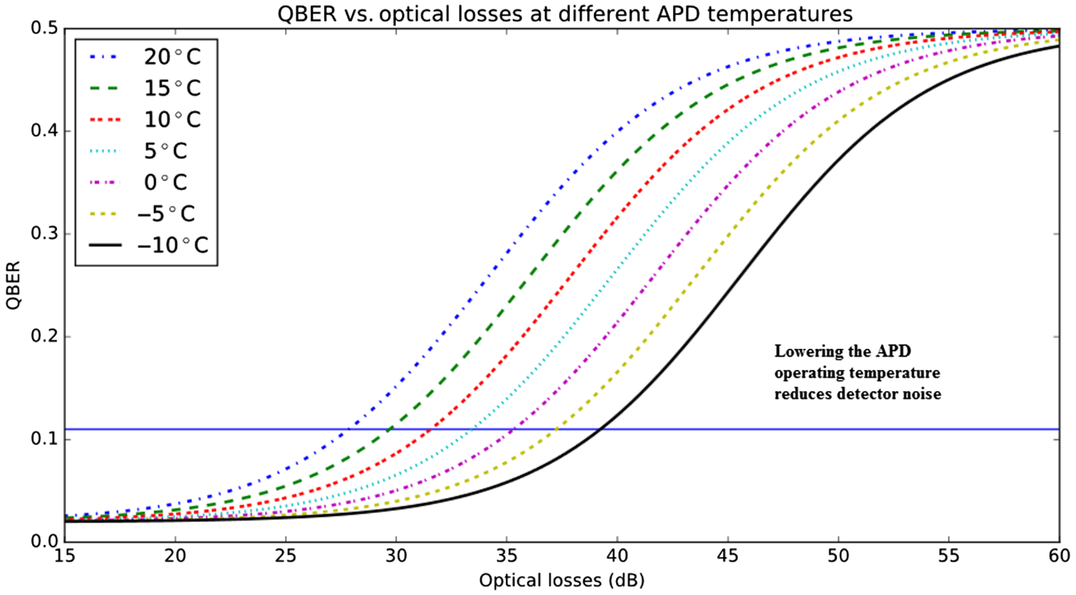

Fig. 6 Optical losses effect on QBER when QM APD detectors are cooled. The horizontal line shows QBER upper limit for BBM92 QKD. QBER never reaches zero because of residual quantum error and depolarization in channel (Based on detector dark count curves and simulations previously reported in Ref. 4).

Background and stray light can significantly reduce the performance of the system if not properly controlled. An initial analysis of the depolarization due to reflections from the optical surfaces produced a negligible reduction in the secure key generation rate. Any detailed system design would need to provide mitigation of predicted stray light levels.

3.1 *Telescope Sizing*

The first step in designing the optical link was to select an aperture for the telescopes that respected the SWaP constraints of the 6U CubeSat and could provide reasonable gain. The on-axis telescope gain is directly proportional to the aperture diameter and inversely proportional to the wavelength, such that $G_T = G_R = (\pi D/\lambda)^2$, where D is the telescope diameter.

Larger apertures produce smaller beam divergences resulting in higher gains, but the power levels measured by a receiver will be more sensitive to beam deflection, because there is more power contained in a narrower beam and the peak intensity can more easily be deflected from the receiver aperture leading to signal fading and dropout. A trade-off between transmitter/receiver gain and uncompensated beam deflection becomes necessary in the design of the optical terminal.

The 6U CubeSat volume limits the size of the telescope, and this impacts the range over which a link can be maintained. The baseline telescope (OTA) is a two-mirror, $F/9$, Ritchey–Chrétien telescope with a clear aperture of 80 mm and a 13% obscuration produced by the secondary mirror. It provides an optical gain of ∼110 dB ($\lambda = 760$ nm) with an assumed average optical transmission factor of 0.7 to account for a worst-case (i.e., end of life) efficiency of the optical coatings.

3.2 *Optical Layout*

The optical design of the payload was created using Zemax OpticStudio®. The size of the active area of the APD detectors in the QM sets a limit on the maximum angular beam deflection that can be tolerated before the transmitted photons would no longer strike the APD. The APD has an active area with a diameter of ∼0.5 mm and the QM coupling lens is an achromatic doublet with a focal length of 50 mm. The optical layout for the QM channel is shown in Fig. 7, where the received beam is collected by the OTA and relayed to the FSM and dichroic mirror and then into the QM.

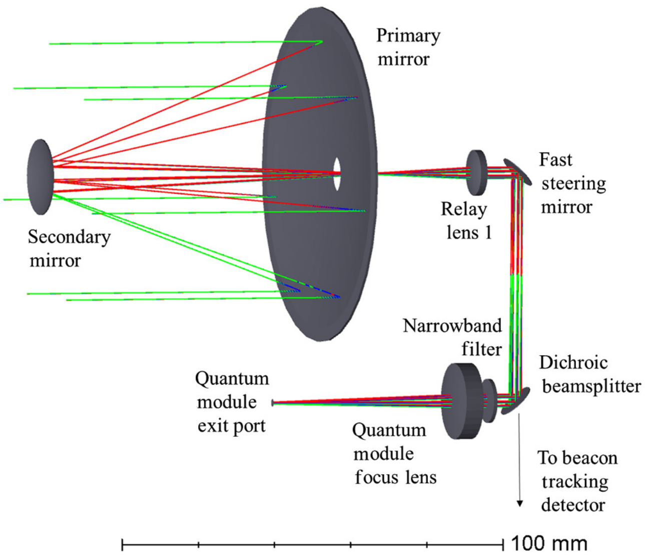

Fig. 7 Optical layout of quantum channel; $\lambda = 760$ nm; internal optics of QM, including 50-mm lens focus at APD are not shown; on-axis and ±0.01 deg off-axis rays are traced using Zemax OpticStudio®.

Although the quantum signals are individual photons, their propagation in this context can be analyzed classically to show that if the deflection of the received quantum beam is within ±175 μrad (±0.01 deg), then a lateral beam displacement on the APD of $\sim \pm 0.23$ mm is produced ensuring the photons strike the APD. A larger beam deflection would cause the photons to arrive outside of the APD active area (in the absence of beam pointing correction). The spacecraft ADCS has a pointing uncertainty of ∼52 μrad, which is within the uncorrected limit of the system to transmit the received photons to the APDs. However, the predicted channel attenuation given by the link equation and the allowable QBER provides the true requirement for the overall uncompensated pointing error.

3.3 *Beam Pointing*

When a laser beam traveling between the transmitter and receiver is deflected, the received optical power is reduced as the Gaussian intensity profile is shifted across the receiver aperture. The intensity of the signal at the receiver can be described as a convolution of the beam intensity and a function of the circular receiver aperture in the local radial coordinate of the aperture, r, and the range, R, between the terminals.

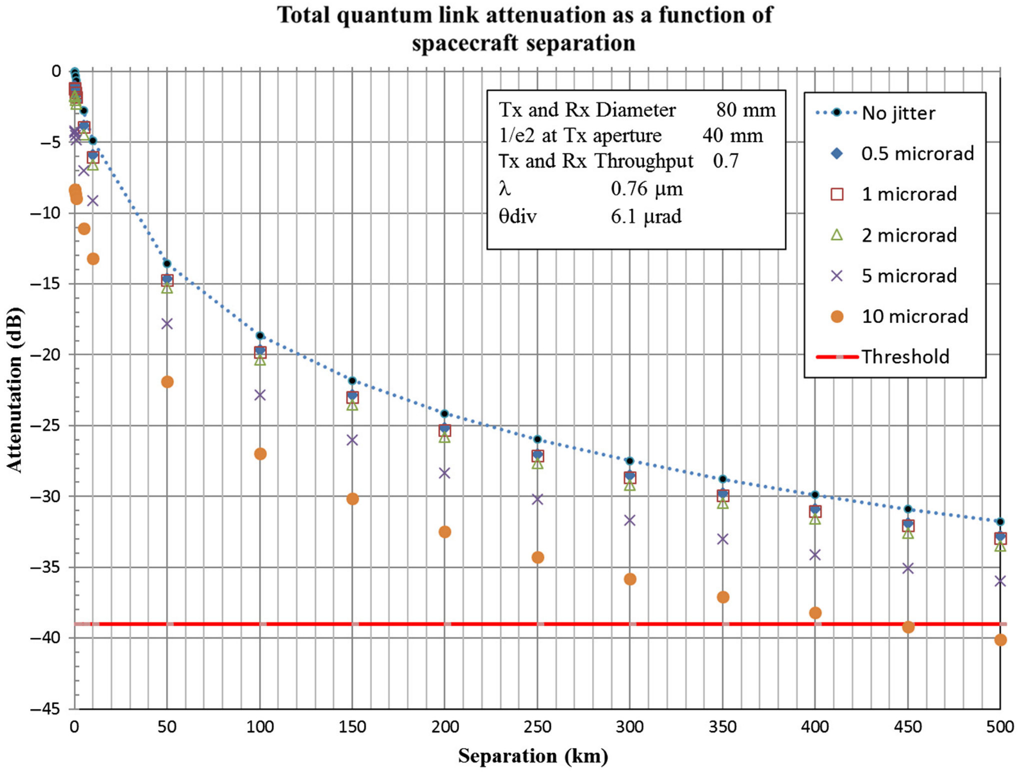

Fig. 8 Total link attenuation as a function of spacecraft separation and beam pointing error. APD temperature is assumed to be −10°C, the horizontal threshold line indicates a QBER = 11%.

Figure 8 shows the total attenuation in the optical channel as a function of range for a transmitter/receiver pair with an 80-mm aperture in the presence of uncompensated beam jitter. The attenuation is computed for the cases with rms beam jitter of 0, 0.5, 1.0, 2.0, 5.0, and 10 μrad. The beam divergence ($\lambda = 760$ nm) is 6.1 μrad at the $1/e^2$ intensity values of the peak of the Gaussian beam intensity. The beam divergence is half of the full beam angular dimension. The pointing error loss was modeled as a two-dimensional (2-D) convolution of the Gaussian beam diffraction intensity profile, and the receiver aperture to calculate the final received power at the detector.[44,45] The red horizontal line represents a link attenuation of 39 dB, which corresponds to the QBER threshold of 11% in our system.

In the absence of other system perturbations, and if closed-loop tracking can be maintained, a QKD link could be established up to 400 km if an uncompensated beam pointing error of 10 μrad can be achieved. In this separation limit, the QBER is just below 11% and the key rate is almost zero.

As the CubeSat body pointing capability provided by the ADCS cannot, by itself, meet such pointing and tracking requirements a dedicated fine pointing capability is needed. Appendix A describes an architecture that uses a laser beacon, a BTD, and an FSM to provide fine angular beam control. Further design iterations of this subsystem will be required, however, for it to function reliably at distances beyond 150 km as the SNR of the measured tracking signal is currently too low at this range.

4 Conclusions

The design and analysis of a compact inter-CubeSat optical link system to support QKD operations have been discussed. Such a system would be a pathfinder for larger systems for QKD satellite constellations. The results indicate that an optical link supporting QKD operations over separation ranges up to ∼400 km is feasible for two 6U sized spacecraft with 80-mm diameter telescopes provided a suitable tracking system can be implemented and assuming uncompensated pointing errors of ∼10 μrad (or better) can be achieved.

For our initial tracking system design, the receiver beacon SNR is ∼10 at 150 km separation, ∼7 at 170 km, and <2 at 400 km, so tracking at distances >150 km becomes challenging and QKD operations beyond that range could not be guaranteed. To increase the usable range, a beacon laser with higher lasing power emitting at commercially available wavelengths (e.g., 1550 nm) could be used.

Other trade-offs can be considered to extend the separation range. For example, if the system could provide an uncompensated pointing error of 5 μrad, then the QBER can be maintained below threshold over extended separations. Active cooling of the APDs with thermoelectric coolers would reduce noise in the detectors, and if the bidirectional QKD requirement were dropped then the QM could be made smaller and larger diameter telescopes might be easier to implement in the expanded spacecraft volume. Alternative, higher brightness quantum light sources could also be sought.

Ultimately, for practical use in constellations, links of thousands of kilometers will be necessary, so larger-form factor satellites will likely be required. A mission such as the one outlined in this paper, however, would still be significant as the first intersatellite QKD link and yet a further demonstration of the increasing capabilities of CubeSat nanosatellites.

5 Appendix A: Pointing Acquisition and Tracking Subsystem

PATS technologies for space-based optical links have been developed over several decades and are being adapted to provide laser communications systems on small spacecraft. In many cases, the data signal is not bright enough to also provide a source for pointing and tracking; therefore, typically a separate "beacon" coaligned with the data signal is used. In this scenario, the receiver can align its LOS vector to the incoming beacon and maintain tracking between the terminals.

High-power laser diodes are typically used as beacons.[46–49] Our PATS design uses a dedicated beacon laser with its own transmitter telescope to optimize the beam pattern at the receiver aperture. The larger, OTA system serves as the receiver for the beacon signal. This "bistatic" design reduces the optomechanical complexity of the system while maintaining the spectral separation of the beacon and quantum beams.

Errors in angular beam alignment caused by mechanical disturbances coupled into the spacecraft structure by vibrations of RW, and other mechanisms decrease the strength of the received signal and can produce data drop outs and signal fading as the transmitted optical beam wanders away from the receiver aperture.

Traditional laser communications systems have a coarse and fine pointing capability and, depending on the application, a point ahead mechanism to steer the optical beam between the terminals. The SWaP constraints of a CubeSat limit the implementation of a robust PATS and hence reduce the overall uncompensated beam pointing that can be achieved. The baseline PATS relies on the blind-body pointing of the spacecraft to provide coarse beam pointing and on a single two-axis FSM to perform fine pointing.

In the beacon acquisition phase, the PATS will contend with large open-loop pointing errors and the two terminals will acquire each other using a master-slave procedure that relies solely on the GPS, two-line element datasets, and ADCS data. The position of the receiver (slave) is known with an uncertainty limited by the uncertainty in the GPS data providing its position information. The transmitter (master) terminal directs its beacon toward the receiver, where the beam width covers this uncertainty zone around the location of the receiver. As the slave terminal detects the beacon, which can be a continuous-wave or modulated output, the PATS slowly adjusts its orientation to maximize the received light and position the beacon at the center of a BTD array. After a defined time, the receiver turns on its beacon, and the former transmitter adjusts its LOS with its PATS to maximize the beacon signal it is detecting. A second fine acquisition phase corrects for small angle deviations in which both master and slave align their FSMs quickly, by scanning simultaneously until mutual tracking is undertaken. In our design, the beacon and the QM have the fine steering mirror in common. This arrangement reduces the alignment error that might arise from a design where a separate deflection element is used for the beacon channel.

5.1 *Optical Beacon*

The optical beacon subsystems include a laser diode, relay optics, optical fiber, and a second, smaller telescope—the Beacon Telescope Assembly (BTA). The diameter of the BTA is chosen such that the projected beam covers an area larger than the predicted location zone of the partner spacecraft beyond the minimum desired operation distance. In the baseline configuration, the beacon laser module includes temperature-controlled laser diode driver circuitry and control electronics. An optical fiber coupled to the output of the laser diode package is routed through the spacecraft to the focus of the BTA, which is mounted on the OTA metering structure and coaligned to the OTA optical axis.

Several commercially available laser diode modules with varying output powers and wavelengths were considered. The baseline beacon is a commercially available 785 nm, 250 mW Fabry–Perot laser diode integrated in a 14-pin butterfly package. The module contains an integrated thermoelectric cooler (TEC), thermistor, and laser output monitor photodiode. The laser output is coupled into a 1-m-long polarization preserving fiber, which has a loss factor of −3.5 dB/km. The output power is lower than typical telecommunications lasers, but a laser that emits in the visible spectrum is easier to align. A beacon at 785 nm is also ideal for generating photocurrent in silicon, where the normalized responsivity is at its peak. It will not, however, allow the QM units to be operated where the 867-nm idler photons are chosen for transmission. In the baseline configuration, the transmitter/receiver role switching would have to be sacrificed or an alternative design arrangement sought, where the beacon wavelength is greater than the entangled photon wavelengths. For example, a telecommunications laser operating at 1550 nm could be used for the beacon.

5.2 *Beacon Telescope*

The beacon telescope projects the beacon light emanating from the optical fiber into space for the partner spacecraft to track. The fiber has a NA of ∼0.13. The baseline beacon telescope is a commercially available fiber-coupled collimator assembly with an NA of ∼0.14, an effective focal length of 60 mm, and a clear aperture of 16 mm. It produces a collimated beam with a width of ∼11 mm and a full divergence angle of ∼90 μrad at 785 nm. Considering transmission losses of the fiber and lens insertion losses an 80% optical path efficiency was assumed yielding an overall gain of ∼92 dB.

The beacon signal transmitted by the BTA on one spacecraft is collected by the OTA on the receiver spacecraft. The optical path layout for this portion of the system is shown in Fig. 9. In addition to a dichroic beam splitter, spectral isolation is provided by two 10-nm narrow bandpass filters (not shown) where one is tuned to 760 nm in the QM path and another tuned to 785 nm in the beacon path. The overall throughput for the beacon receiver optical path is ∼0.6, which includes transmission factors for each of the optical elements.

5.3 *Beacon Detector*

The beacon detector must provide ample sensitivity to detect the imaged beacon while providing fast readout and low noise to produce accurate error correction data to the FSM controller. Several candidates have been investigated including Si-based CCD and CMOS arrays, Si- and InGaAs quadrant detectors, and position sensing detectors.[26,50]

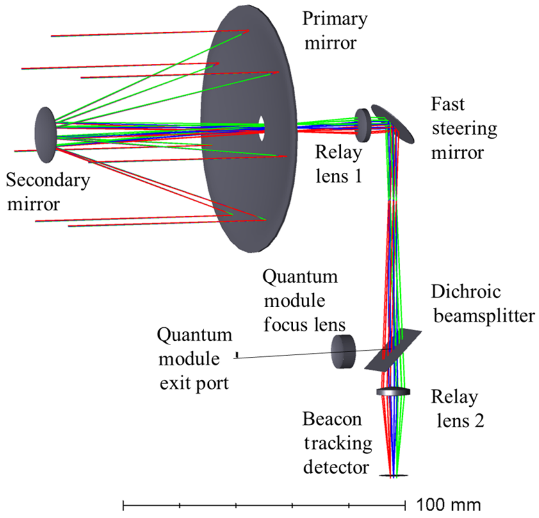

Fig. 9 PATS beacon detector optical path; on-axis and off-axis (±0.05 deg) rays are traced using Zemax OpticStudio®.

The preliminary design uses a commercially available CMOS array. Reasonable pixel size, dynamic range, and readout rate were key design drivers. For the PATS system, a minimum frame rate of ∼50 to 100 Hz is needed to achieve adequate beacon tracking. The baseline detector has global shuttering and region of interest selection capability. The pixel size is ∼4.8 μm providing sufficient sampling of the beacon image point spread function (PSF), which has a full-width of ∼25 μm on-axis. The array active area is ∼3.6 mm × 2.7 mm.

In a receiver mode, a 5 μrad angular offset in the incoming beam yields a shift of the beacon image centroid of ∼5.2 μm (slightly >1.2 pixels). A one-pixel centroid offset provides a conservative indication of the minimum uncompensated pointing error correction that the PATS can achieve. For the baseline, this value is then ∼5 μrad. Subpixel motion detection may be possible, but the total system noise must first be assessed.

The beacon detector field of regard (FOR) is limited by the physical size of the array and any vignetting in the optical path. The SWaP constraints of the spacecraft limit the size of the optical components that can be accommodated. In the baseline configuration, a ±0.1 deg (±1.75 milliradians) angular deflection produces almost 50% vignetting of the beacon beam. When the beam deflection is kept below ±0.06 deg (±1.0 milliradians) there is no vignetting (which is the case in closed-loop tracking). During open-loop acquisition, some beam vignetting may be incurred; however, during closed-loop tracking no vignetting of the beacon occurs. Correcting for beam jitter with a resolution of 5 μrad ensures the received photons will fall on the APD active area.

5.4 *Beacon Deflection Sensitivity*

The optical components and detector are sized, so that the receiver can acquire the transmitter beacon in a open-loop mode without additional scanning. For example, at a range of 50 km, the BTD dimensions are projected into a zone that would have ~0.23-km diagonal. Given the uncertainty in the GPS location of the two spacecraft and uncertainty in the AOCS pointing capability (which is estimated at 52 μrad $1-\sigma$), the BTD on the receiver spacecraft should still see the transmitted beacon without the need for raster scanning by the FSM.

Even with the worst-case uncertainty in pointing and location of the two spacecraft, the BTD FOR can capture a point source that is up to ±0.1- deg off-axis. In addition to acquiring the beacon, the BTD must also sense when the beacon angular position varies. The link analysis of the optical channel showed that a maximum uncompensated pointing jitter of ~ 10 μrad can be tolerated. The BTD has a pixel plate scale of ~ 5.1 μrad/pixel. This is the minimum beam deflection that can be sensed, and the FSM must provide at least this level of steering accuracy to yield a system capable of maintaining alignment between the spacecraft. The uncertainty in the pointing capability of the baseline AOCS would result in a beacon image displacement at the detector of ~ 23 μm. This multiple pixel displacement should be easily detected.

5.5 *Fast Steering Mirror*

A central element of the PATS is the FSM. The FSM provides beam pointing compensation and scanning capability. Several commercially available two-axis fast-steering mirrors with angular resolutions of <1 μrad have been considered. The baseline FSM contains an 18-mm × 24-mm glass substrate with a high-reflectance coating having a rms wavefront error of $<\lambda/4$ @ 633 nm. The FSM actuator mechanism has a travel range of up to 160 milliradians and a step size in closed-loop operation of 1.0 μrad with a total induced jitter of 0.7 μrad rms. The closed-loop servo bandwidth is ~ 350 Hz.

5.6 *Beam Control*

The control bandwidth of the FSM servo system will depend on the actual spacecraft disturbance spectrum. A preliminary analysis shows that the frequency disturbance due to AOCS single reaction-wheel imbalance at 3000 rpm is ~ 3 μrad at 60 Hz. A passive isolation system can be used as a possible feature of the PATS, depending on other trade-offs.

The main PATS hardware elements are shown in Fig. 9. The received light is acquired by the OTA and recollimated by relay lens 1. The beam then reflects from the FSM to the dichroic beamsplitter (DBS), which transmits light >770 nm to relay lens 2, which focuses the beam onto the BTD. The DBS reflects light with wavelength <770 nm to the QM.

The centroid of the beacon image is calculated by the detector readout electronics and fed to a proportional integral derivative (PID) controller. The PID control signals are sent to the FSM driver to change the angular position of the FSM in response to input beam angular deflections. The focused beacon beam is steered to stabilize the beacon image at the pixel corresponding to the LOS of the receiver optical path.[51] The detector can operate at full-frame readout rates up to 545 fps at 10 bits/pixel. Performance should be improved by implementing subpixel tracking error compensation. A breadboard system is being constructed at UNSW Canberra to validate tracking models and determine sensitivities for the PATS.

5.7 *Control Loop Limitations*

The total tracking error will be the sum of the uncompensated error plus any noise-induced error. The noise equivalent angle (NEA) is that angle that cannot be corrected due to all noise sources present in the system. As the NEA is a combination of error sources including the detector noise, beacon brightness variations, PATS noise, and statistical uncertainties in beam centroid computations, the frequency characteristics of all these terms must be considered with respect to the control bandwidths of the elements comprising the PATS. It will be important to understand the proportion of the total disturbances that are not corrected as well the fraction that are not sensed in determining the total uncompensated pointing error.[52]

A first step in assessing the PATS capability is to estimate the radiative transfer of beacon energy from the transmitting spacecraft to the receiver. In radiometric terms, the receiver at-aperture beacon radiance is transferred along the optical path to form an image at the BTD, which can be described in units of energy per unit area. The energy is converted on a per-pixel basis into photocurrent and then into a digital number (DN), where the range of DN spans the charge capacity of the pixel. The conversion characteristics of the BTD provide the conversion from irradiance to photocurrent and an estimate of the detected beacon SNR. The beacon will appear to the receiver as a point source rather than as an extended object. The ensquared energy of the beacon image formed on the detector predicts that 90% of the energy is contained within an image diameter of ~40 to 50 μm.

The link equation accounts for the expansion of the beacon beam from the transmitter BTA to the aperture of the receiver OTA. The baseline BTA has a gain equal to ~ 95 dB, (where the beam at the $1/e^2$ points just under-fills the BTA aperture). The OTA receiver has a gain of ~ 110 dB, and the optical throughput and QE of the BTD have been used to compute the signal electrons generated by the BTD.

Figure 10 shows a plot of the BTD signal electrons as a function of range between the two spacecraft, where the beacon laser is emitting at a maximum power output of 0.25 W and the BTD frame rate is set to 25 fps with an integration time of 100 μs. The beacon channel SNR remains above 10 for separation distances approaching ~ 100 km. At spacecraft separations of $<\sim 15$ km, the imaged beacon flux would saturate the BTD as the full well capacity is only $\sim 10{,}000$ electrons. At these distances, a lower power setting can be selected.

The loss in beacon signal and the probability of burst errors (PBE) as a function of the beamwidth to rms pointing error ratio produces an estimate equal to $\sim 1 \times 10^{-4}$. To increase the operational range for the system and reduce the PBE even further, a higher power beacon laser can be considered or longer integration times.

The initial concept of operations foresees QKD only being performed while the spacecraft is in eclipse to avoid noise from stray light. However, during operations, the BTD on each spacecraft will see a stellar background. The projection of the array on the sky will be ~ 5 milliradians on the diagonal and at a range of 100 km, the resultant solid angle is $\sim 2 \times 10^{-5}$ sr.

The number of objects brighter than the dimmest detectable object located within a solid angle as seen from the Earth leads to an estimation of the number of objects brighter

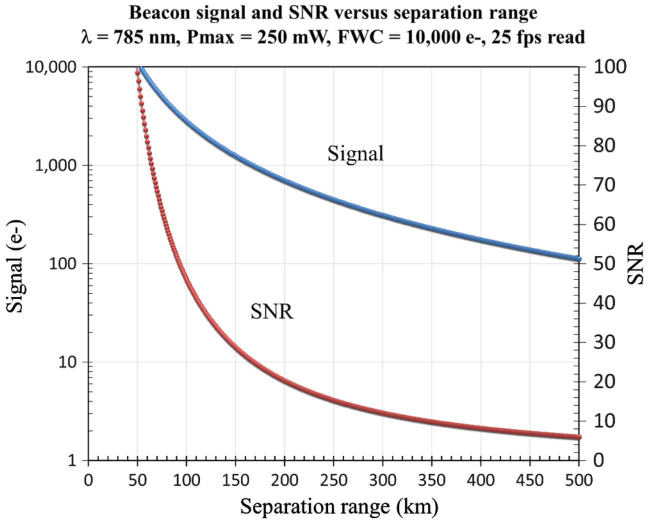

Fig. 10 Beacon signal level and SNR as a function of spacecraft separation.

than the dimmest detectable object. There could be ~1600 objects brighter than the beacon visible from Earth above the hemisphere (National Solar Observatory, Sacramento Peak, California). The sensitivity of the BTD allows stellar objects brighter than apparent visual magnitude 4 to be detected. A simple ratio of the solid angle subtended by the BTD to the hemisphere indicates that there will be virtually no stellar objects bright enough to compete with the beacon. However, the beacon signal can be further isolated from the stellar background using spectral filtering as well as temporal modulation of the beacon laser.

Table 2 Beacon channel link budget; range 100/300 km, $\lambda = 785$ nm, NEA ~ 10 μrad.

Contributor	Parameter	Value
Laser power	250 mW	–6 dB (24 dBm)
Tx optical throughput	70%	–1.5 dB
Tx gain	16 mm ø	95 dB
Free space loss	@ 100 km	–225 dB
	@ 300 km	–253 dB
Rx gain	80 mm ø	115 dB
Rx optical throughput	60%	–2.2 dB
Pointing loss	10 μrad uncompensated Pointing error	–8.0 dB @ 100 km –17.5 dB @ 300 km
	5.0	–3.24 dB
Total link attenuation = –29.7 dB @ 100 km; –70.2 dB @ 300 km		
Detector read noise	Nonillumination related	14 e-
Conversion gain (10 bits)	-	9.1 e- / DN
Minimum detectable signal	~18 e- (~2 DN) $\sim 8 \times 10^{-11}$ W	–101 dB
Margin		71.3 dB @ 100 km
		29.8 dB @ 300 km

5.8 *Centroid Computation Methods*

A preliminary estimate of the beacon centroid error has been computed assuming a simple center-pixel algorithm. The beacon source will be focused to a spot of ~25 μm, which will be oversampled with the 5.5 μm square pixels. Subpixel errors in centroid position estimation are foreseen. Several standard centroid estimating methods are the subjects of ongoing investigations.[53–55]

Table 3 Beacon pointing budget.

Static error source	Allocation (μrad)	Notes
GPS	100	Assuming GPS position uncertainty +/ – 0.5 m for each satellite. Worst case relative uncertainty is 1 m and at $R = 100$ km is an angular uncertainty of ~100 μrad
BTA/OTA pointing offset	100	Alignment uncertainty between LOS of BTA and OTA
AOCS		
ADCS closed loop	52	Manufacturer residual uncertainty about local *x*, *y*, and *z*
Bias uncertainty	±5.0	allocated
Alignment errors	±5.0	allocated
Point ahead angular distance	±1.0	At $R = 100$ km, a S/C moves 2.53 m in the time it takes the beacon/quantum photon to reach it from the transmitter
Total static bias (RSS)	113	BTD FOR can accommodate this static bias
Dynamic error source		
PSF quality	~2.0	Influenced by optical component quality, and centroid algorithm inefficiency (equate to half a pixel)
Pixel to pixel nonuniformity	~2.0	Allocation
Read noise	~4.0	Allocation
Photon noise	~2.0	Allocation
Centroid computation errors	~2.0	Allocation
Uncompensated S/C jitter	±3.0	Calculated RW disturbances
Total dynamic error (RSS)	6.8	Requirement <10 μrad

5.9 *Beacon Link Margin*

Errors in spacecraft location due to uncertainties in the GPS signal are assumed to be on the order of 0.5 to 1.0 m in each axis.[56] The baseline concept of operations relies solely on the body pointing of the spacecraft to acquire the beacon in a open-loop mode. Immediately after separation, the uncertainty in the locations of the two spacecraft will not allow the receiver to acquire a transmitted beacon reliably as the baseline design does not include provision for scanning. So, a minimum spacecraft separation must be reached before the transmitted beam will be within the receiver field of view. A scanning feature could be provided by the ADCS, by the addition of an additional scan mirror, or by using the existing FSM in a scan mode for which a separate scan servo loop would need to be designed.

For an example, a spacecraft separation of 5 km, the beacon beam diameter would be ~ 2 m and would cover the uncertainty zone in which the receiver should be located. The baseline design provides margin for beacon detection for spacecraft separation >100 km. An example beacon link budget is shown in Table 2.

A preliminary pointing budget for the beacon subsystem is shown in Table 3. The estimated static bias errors can be accommodated within the FOR of the BTD. These allocations are preliminary and refinement is ongoing, but the budget is within the derived requirement of 10 μrad uncompensated jitter and less than the plate-scale resolution of the PATS.

The beam pointing margin for the quantum channel can only be as good as that established by the beacon-based PATS. An uncompensated beam deflection of 10 μrad will cause a shift of the received quantum beam on the QM APD of ~ 25 μm, which is well within the sensitive area of the APD detector.

References

1. H. J. Kimble, "The quantum internet," *Nature* **453**(7198), 1023–1030 (2008).
2. D. Rideout et al., "Fundamental quantum optics experiments conceivable with satellites reaching relativistic distances and velocities," *Classical Quantum Gravity* **29**(22), 224011 (2012).
3. D. K. Oi et al., "CubeSat quantum communications mission," *EPJ Quantum Technol.* **4**, 6 (2017).
4. R. Bedington et al., "Progress in satellite quantum key distribution," *NPG Quantum Inf.* **3**, 30 (2017).
5. S. Pirandola et al., "Fundamental limits of repeater-less quantum communications," *Nat. Commun.* **8**, 15043 (2017).
6. H. L. Yin et al., "Measurement-device-independent quantum key distribution over a 404 km optical fiber," *Phys. Rev. Lett.* **117**, 190501 (2016).
7. A. R. Dixon et al., "High speed prototype quantum key distribution system and long term field trial," *Opt. Express* **23**(6), 7583–7592 (2015).
8. S.-K. Liao et al., "Satellite-to-ground quantum key distribution," *Nature* **549**, 43–47 (2017).
9. K. Günthner et al., "Quantum-limited measurements of optical signals from a geostationary satellite," *Optica* **4**(6), 611–616 (2017).
10. H. Takenaka et al., "Satellite-to-ground quantum-limited communication using a 50-kg-class microsatellite," *Nat. Photonics* **11**, 502–508 (2017).
11. E. Gibney, "Chinese satellite is one giant step for the quantum internet," *Nature* **535**(7613), 478–479 (2016).
12. R. Bedington et al., "Nanosatellite experiments to enable future space-based QKD missions," *EPJ Quantum Technol.* **3**, 12 (2016).
13. J. M. P. Armengol et al., "Quantum communications at ESA: towards a space experiment on the ISS," *Acta Astronaut.* **63**, 165–178 (2008).
14. M. Aspelmeyer et al., "Long-distance quantum communications with entangled photons using small satellites," *IEEE J. Sel. Top. Quantum Electron.* **9**(6), 1541–1551 (2003).
15. N. Gisin et al., "Quantum cryptography," *Rev. Mod. Phys.* **74**(1), 145–195 (2002).
16. E. Diamanti et al., "Practical challenges in quantum key distribution," *NPJ Quantum Inf.* **2**(1), 16025 (2016).
17. V. Scarani et al., "The security of practical quantum key distribution," *Rev. Mod. Phys.* **81**(3), 1301–1350 (2009).
18. C. Ho, A. Lamas-Linares, and C. Kurtsiefer, "Clock synchronization by remote detection of correlated photon pairs," *New J. Phys.* **11**, 045011 (2009).
19. C. H. Bennett, G. Brassard, and N. D. Mermin, "Quantum cryptography without Bell's theorem," *Phys. Rev. Lett.* **68**(5), 557–559 (1992).
20. C. H. Bennett and G. Brassard, "Quantum cryptography: public key distribution and coin tossing," in *Proc. of IEEE Int. Conf. on Computers Systems and Signal Processing*, Vol. **1** (1984).
21. J. Yin et al., "Satellite-based entanglement distribution over 1200 kilometres," *Science* **356**(6343), 1140–1144 (2017).
22. J. Yin et al., "Satellite-to-ground entanglement-based quantum key distribution," *Phys. Rev. Lett.* **119**(20), 200501 (2017).
23. H. Kaushal and G. Kaddoum, "Optical communication in space: challenges and mitigation techniques," *IEEE Commun. Surv. Tutorials* **19**(1), 57–96 (2017).
24. F. Moll et al., "Aerospace laser communications technology as enabler for worldwide quantum key distribution," *Proc. SPIE* **9900**, 990001 (2016).
25. M. Guelman et al., "Acquisition and pointing control for inter-satellite laser communications," *IEEE Trans. Aerosp. Electron. Syst.* **40**(4), 1239–1248 (2004).
26. J. Takashi, "Acquisition, tracking and pointing systems of OICETS for free space laser communications," *Proc. SPIE* **3692**, 41–50 (1999).
27. G. Planche et al., "Silex final ground testing and in-flight performance assessments," *Proc. SPIE* **3615**, 64–77 (1999).
28. T. S. Rose et al., "LEO to ground optical communications from a small satellite platform," *Proc. SPIE* **9354**, 93540I (2015).
29. E. Clements et al., "Nanosatellite optical downlink experiment: design, simulations and prototyping," *Opt. Eng.* **55**(11), 111610 (2016).
30. R. Morgan and K. Cahoy, "Nanosatellite lasercom system," in *AIAA/USU Conf. on Small Satellites*, Technical Session 8 (2017).
31. S.-K. Liao et al., "Long-distance free-space quantum key distribution in daylight towards inter-satellite communication," *Nat. Photonics* **11**, 509–513 (2017).
32. L. O. Mailloux et al., "System-level considerations for modeling space-based quantum key distribution architectures," in *Annual IEEE Int. Systems Conf.*, pp. 2472–9647 (2017).
33. B. Smith et al., "Investigation into the practicability of differential lift-based spacecraft rendezvous," *J. Guid. Control Dyn.* **40**(10), 2682–2689 (2017).
34. P. W. Shor and J. Preskill, "Simple proof of security of the BB84 quantum key distribution protocol," *Phys. Rev. Lett.* **85**(2), 441–444 (2000).
35. M. P. Peloso et al., "Daylight operation of a free space, entanglement-based quantum key distribution system," *New J. Phys.* **11**(4), 045007 (2009).
36. M. T. Gruneisen et al., "Modeling daytime sky access for a satellite quantum key distribution downlink," *Opt. Express* **23**(18), 23924–23934 (2015).
37. R. C. M. R. B. Chandrasekara et al., "Demonstrating miniaturized, entangled photon-pair sources on board nanosatellites to enable future QKD missions," in *68th Int. Astronautical Congress (IAC)*, Adelaide, Australia, IAC-17-B2.7.2 (2017).
38. P. Trojek and H. Weinfurter, "Collinear source of polarisation-entangled photon pairs at nondegenerate wavelengths," *Appl. Phys. Lett.* **92**(21), 211103 (2008).
39. ESATAN-TMS, *Workbench User Manual*, ITP Engines UK Ltd., Whetstone, Leicester (2009).
40. Y. C. Tan et al., "Silicon avalanche photodiode operation and lifetime analysis for small satellites," *Opt. Express* **21**(14), 16946–16954 (2013).
41. T. Islam, R. Bedington, and A. Ling, "Approaches to a global quantum key distribution network," *Proc. SPIE* **10442**, 1044208 (2017).
42. T. Vértesi, "More efficient Bell inequalities for Werner states," *Phys. Rev. A* **78**(3), 032112 (2008).
43. B. Klein and J. Degnan, "Optical antenna gain. 1: transmitting antennas," *Appl. Opt.* **13**(9), 2134–2141 (1974).
44. B. Boone et al., "Optical communications development for spacecraft applications: recent progress at JHU/APL," in *IEEE Aerospace Conf.*, Big Sky, Montana, 1559448 (2005).
45. W. K. Marshall, "Transmitter pointing loss calculation for free-space optical communication link analyses," *Appl. Opt.* **26**(11), 2055–2057 (1987).
46. K. Held and D. Barry, "Precision optical pointing and tracking from spacecraft with vibrational noise," *Proc. SPIE* **616**, 160–173 (1986).
47. C. Chen and C. Gardner, "Impact of random pointing and tracking errors on the design of coherent and incoherent optical inter-satellite communication links," *IEEE Trans. Commun.* **37**(3), 252–260 (1989).
48. T. Nguyen et al., "Development of a pointing, acquisition and tracking system for a CubeSat optical communication module," *Proc. SPIE* **9354**, 93540O (2015).
49. H. Henniger and O. Wilfert, "An introduction to free-space optical communications," *Radioengineering* **19**(2), 203–212 (2010).
50. E. Swanson and J. Roberge, "Design considerations and experimental results for direct-detection spatial tracking systems," *Opt. Eng.* **28**(6), 286659 (1989).

51. T. Shimizu et al., "Image stabilization system for Hinode (Solar-B) solar optical telescope," *Sol. Phys.* **249**(2), 221–232 (2008).
52. J. D. Barry and G. S. Mecherle, "Beam pointing error as a significant design parameter for satellite-borne, free-space optical communication systems," *Opt. Eng.* **24**(6), 1049–1054 (1985).
53. S. Thomas, "Comparison of centroid computation algorithms in a Shack-Hartmann sensor," *Mon. Not. R. Astron. Soc.* **371**(1), 323–336 (2006).
54. C. Mendillo et al., "Flight demonstration of a milliarcsecond pointing system for direct exoplanet imaging," *Appl. Opt.* **51**(29), 7069–7079 (2012).
55. T. Delabie, "An accurate and efficient Gaussian fit centroiding algorithm for star trackers," *J. Astronaut. Sci.* **61**(1), 60–84 (2014).
56. J. Gangestad, B. Hardy, and D. Hinkly, "Operations, orbit determination and formation control of the AeroCube-4 CubeSat," in *27th AIAA/USU Conf. on Small Satellites*, Provo, Utah, SSC13-X-4 (2014).

Denis Naughton is a system engineer employed at the University of New South Wales, Canberra. He received his BS degree in physics from Catholic University of America and his MS degree in optical engineering from the University of Rochester. He has over 20 years of experience in the development and calibration of electro-optic payloads for Earth observation missions. He is a member of SPIE.

Robert Bedington is a senior research fellow employed at the National University of Singapore, Centre for Quantum Technologies. He received his MSci degree in physics from the University of Durham and his PhD in space instrumentation from the University College London, Mullard Space Science Laboratory. He has over 10 years of experience working on the miniaturization of space instrumentation.

Simon Barraclough is a system engineer and mission manager at UNSW Canberra Space. Currently, he is the project lead for the UNSW M1 mission. He has over 20 years of experience in the aerospace industry with 17 years spent at Airbus Defence and Space UK, where he was a thermal engineer and group leader in support of ESA missions including Rosetta, LISA Pathfinder, Mars, and Venus Express, Aeolus and the upcoming Solar Orbiter.

Israel J. Vaughn completed his BS degree in mathematics from New Mexico Tech, his MS degree in mathematics from the University of New Mexico, and his PhD in optical sciences from the University of Arizona. Currently, he is a research associate in the School of Engineering and Information Technology at UNSW Canberra. His research focuses on optical wavelength polarimetric sensing technologies, imaging science, space surveillance technologies, hybrid spectro-polarimetric imaging technologies, and general optical instrumentation.

Biographies for the other authors are not available.